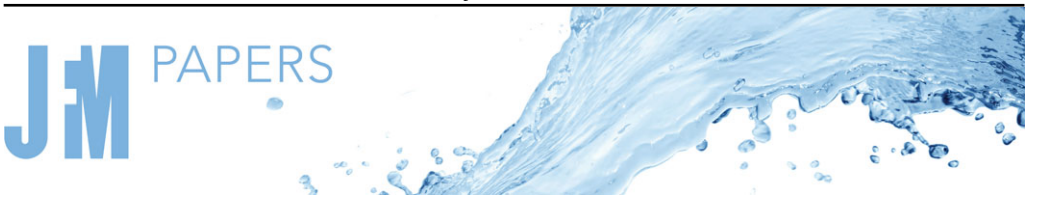
J. Fluid Mech. (2025), *vol.* 1010, A16, doi:10.1017/jfm.2025.282



Quasi-steady shock refraction phenomenon at a diffusive fast–slow interface

Jingqian Pu[1], **Ben Guan**[2], **Zhiwei Deng**[2], **Zhigang Zhai**[1] and **Xisheng Luo**[1,3]

[1]Advanced Propulsion Laboratory, Department of Modern Mechanics, University of Science and Technology of China, Hefei 230026, PR China

[2]College of Aerospace and Civil Engineering, Harbin Engineering University, Heilongjiang 150001, PR China

[3]State Key Laboratory of High Temperature Gas Dynamics, Institute of Mechanics, Chinese Academy of Sciences, Beijing 100190, PR China

Corresponding author: Zhigang Zhai, sanjing@ustc.edu.cn

(Received 4 December 2024; revised 17 February 2025; accepted 9 March 2025)

The quasi-steady shock refraction at a diffusive air–SF_6 interface (fast–slow type) is investigated numerically and theoretically. A new refraction pattern where both shock and expansion waves are simultaneously present in the reflected waves (named RRR-E) is first observed at the diffusive interface. The new refraction pattern is a regular pattern that is not expected to occur in classical shock refraction at a sharp fast–slow interface. Through the shock polar method, continuous refraction processes occur within the diffusion layer to satisfy the kinematic relationship between the reflected wave and the transmitted shock, which results in the RRR-E formation. Subsequently, the conditions for the RRR-E occurrence are obtained theoretically and verified numerically. In the phase diagram of the refraction patterns, the presence of RRR-E results in the transition boundaries of different refraction patterns at the sharp fast–slow interface no longer being valid. Specifically, the appearance of RRR-E delays the Mach reflection refraction (MRR) process, which is of great significance for the design of scramjet engines.

Key words: shock waves

1. Introduction

When a moving shock wave strikes at an interface separating different materials, both reflection and refraction take place simultaneously. The transmitted wave is always a shock, while the reflected wave may be a shock or an expansion wave. If the incident shock, transmitted shock and reflected wave meet all at the same point on the interface,

© The Author(s), 2025. Published by Cambridge University Press.

https://doi.org/10.1017/jfm.2025.282 Published online by Cambridge University Press

and the flow between any two adjacent waves is uniform, then the refraction is called regular refraction. On the contrary, if the flow between adjacent waves is not uniform everywhere, then it is called irregular refraction (Ben-Dor *et al.* 2000). The property of shock refraction is dependent upon the intensity of the incident shock, the angle between the incident shock and the interface (incident angle hereinafter), and the properties of materials on both sides of the interface.

Shock refraction occurs in many fields of science, such as shock–boundary layer interaction on transonic aerofoils (Szubert *et al.* 2015; Sabnis & Babinsky 2023), blast wave reflection and refraction at the water surface (Arun Kumar *et al.* 2022; Raj *et al.* 2024), shock interaction with flame fronts (Yang & Radulescu 2021), shock propagation in an abrupt expanded duct (Gichon *et al.* 2024), and flow instabilities in inertial confinement fusion (Wheatley *et al.* 2005; Delmont *et al.* 2009; Zhang *et al.* 2024). Specifically, shock refraction has great significance in the design of supersonic vehicles. In the scramjet engine, fuel is injected into the combustion chamber and undergoes multiple interactions with the complex waves. By reasonably designing the engine configuration, the combustion efficiency can be greatly improved (Urzay 2018). In addition, through deploying a laser pulse at the nose of a supersonic aircraft, the structure of the bow shock at the front of the aircraft can be changed using the thermal decomposition of air caused by the laser pulse, which can significantly reduce the drag induced by the shock wave (Elias *et al.* 2018). This can, in turn, alleviate the shock effects during supersonic flight, and the heating issues during re-entry into the atmosphere (Markhotok *et al.* 2008; Markhotok & Popovic 2010).

Due to the diversity of material components, the incident angle, and the intensity of the incident shock wave, the refraction of the shock wave at the interface will form a variety of wave structures (Han & Yin 1993). Because the phenomena of shock refraction at a gaseous interface are very complicated, especially for irregular refraction patterns, it is difficult to obtain the analytical solutions, and the simplified models were generally adopted to study shock refraction phenomena. Based on the three-shock theory (Von Neumann 1943; Taub 1947; Polachek & Seeger 1951), Henderson (1966) established the refraction theory for regular refraction with a reflected shock by considering the gas interface as an infinitely thin sharp one, and simplified the motion equations into a single polynomial equation of degree 12. Subsequently, the regular refraction theory for reflected expansion waves was supplemented (Henderson 1967*a*), making the characterisation of refraction patterns more accurate. By establishing a mapping between the shock structure and the polar curves, Henderson (1967*a*) conducted a detailed discussion on the classification and transition of the wave patterns.

According to the physical properties of the materials, the interface can be divided into two types: ‘fast–slow’ and ‘slow–fast’. The so-called ‘fast–slow’ type means that the speed of sound of the material in which the incident shock moves is greater than that in which the transmitted shock moves (e.g. air–SF_6, helium–CO_2). If the speed of sound in the incident material is less than that in the transmitted material, then the interface is referred to as ‘slow–fast’ (e.g. CO_2–CH_4, air–helium). Relatively, the refraction patterns at a ‘slow–fast’ interface (Abd-El-Fattah & Henderson 1978*a*; Takayama & Ben-Dor 1989; Zhai *et al.* 2014, 2017; Luo *et al.* 2015) are much more complicated than those at a ‘fast–slow’ interface (Abd-El-Fattah & Henderson 1978*b*). For ‘fast–slow’ interfaces, the shock polar method and experiments were used to investigate the refraction patterns at air–SF_6 and helium–CO_2 interfaces (Abd-El-Fattah & Henderson 1978*b*). The various shock angles and flow deflection angles were measured, and a phase diagram for the refraction patterns at the air–SF_6 interface was constructed. Five different wave patterns were observed at ‘fast–slow’ interfaces: regular refraction with a reflected shock wave (RRR), regular refraction with a reflected expansion wave (RRE), centred expansion refraction (CER),

https://doi.org/10.1017/jfm.2025.282 Published online by Cambridge University Press

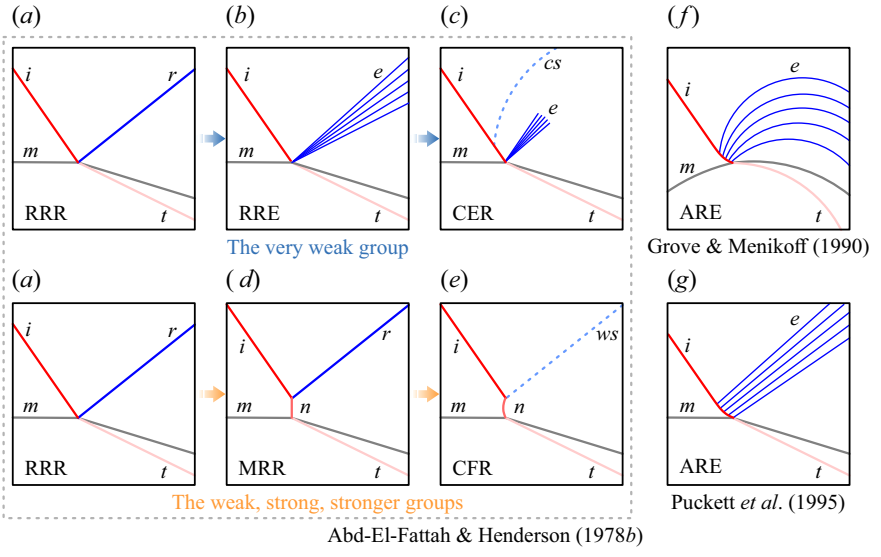


Figure 1. Schematic diagram of shock refraction at a 'fast–slow' interface: *i*, incident shock; *r*, reflected shock; *t*, transmitted shock; *e*, expansion wave; *n*, Mach stem; *cs*, corner signal; *ws*, weak shock; *m*, the material interface.

Mach reflection refraction (MRR), and concave forwards refraction (CFR). For clarity and better description, these five different refraction patterns are illustrated in figures 1(*a*) to 1(*e*), respectively. The RRR pattern is characterised by the incident shock, reflected shock and transmitted shock intersecting at the same point on the interface. In RRE, the reflected wave becomes an expansion wave. The CER pattern features a corner signal on the incident shock, and a centred expansion wave at its base. The MRR pattern resembles Mach reflection, with a Mach stem between the incident shock and the interface. The CFR pattern is similar to MRR, but has a forward-bulging incident shock base and a weaker reflected shock. In general, for different shock intensities, the refraction has different flow patterns. In terms of incident shock intensity, the refraction patterns within the 'fast–slow' group were divided into four classes: very weak, weak, strong and stronger (Abd-El-Fattah & Henderson 1978*b*).

In the work of Abd-El-Fattah & Henderson (1978*b*), three refraction patterns, RRR, RRE and CER, were observed in succession as the incident angle increases in the very weak incident shock group ($\xi_i = p_0/p_1 = 0.909$, the ratio of pressure ahead of and behind the incident shock). In the weak ($\xi_i = 0.66$), strong ($\xi_i = 0.25$) and stronger ($\xi_i = 0.143$) incident shock groups, the refraction patterns observed were RRR, MRR and CFR. However, the distribution of CER was missing in the phase diagram created by Abd-El-Fattah & Henderson (1978*b*), and CFR occurs in the region where CER should be. Although the flow Mach number behind the incident shock (M_1) in both CER and CFR satisfies $M_1 < 1$, the reasons for generating these two refraction patterns are entirely different. In CER, the polar envelope of the transmitted shock is outside the polar envelope of the incident shock, and there are no intersections between them, as illustrated in figure 2(*a*). An expansion wave polar originating from the sonic point *s* intersects with the transmitted shock polar at point *C*. In CFR, however, there are intersection points between the transmitted and incident shock polars, as shown in figure 2(*b*). At this moment, the envelope of the reflected shock polar *r* will degenerate into a point on the shock polar diagram, which is an extreme case.

https://doi.org/10.1017/jfm.2025.282 Published online by Cambridge University Press

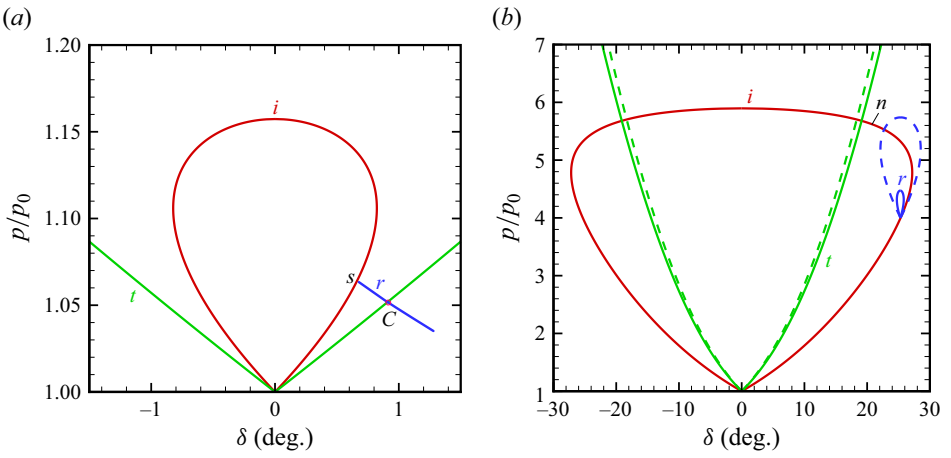


Figure 2. The shock polar diagrams of (*a*) CER with $\xi_i = 0.909$ and $\omega_0 = 78°$, and (*b*) the transition process from MRR to CFR. The green dashed line represents MRR when $\xi_i = 0.25$ and $\omega_0 = 55°$, while the green solid line represents MRR when $\xi_i = 0.25$ and $\omega_0 = 60°$. Here, ξ_i is the ratio of pressure ahead of and behind the incident shock, ω_0 is the incident angle; s is the sonic point, and C indicates the intersection point of the reflected expansion wave and the transmitted shock polars.

In addition to the refraction patterns mentioned by Abd-El-Fattah & Henderson (1978*b*), Grove & Menikoff (1990) numerically investigated the refraction of a planar shock wave at the water–air interface, and observed an anomalous refraction (ARE): a transition from regular reflection to Mach reflection could also occur when the reflected wave is an expansion wave, as illustrated in figure 1(*f*). It is characterised by a curvature at the base of the incident shock, from which expansion waves are emitted. The ARE formation is ascribed to the curvature of the shock wave or interface, which causes the flow behind the incident shock to become subsonic, leading to a bifurcation of the shock node and interference at the base of the incident shock by the reflected expansion waves. Subsequently, Puckett *et al.* (1995) proposed that the backward curvature at the base of the incident shock wave was due to the local weakening by expansion waves. They also numerically simulated the quasi-steady refraction process at the air–CO_2 interface, reproducing the CER pattern observed by Abd-El-Fattah & Henderson (1978*b*). In fact, a series of dispersed expansion bands, rather than a single centred expansion wave, occurs behind the incident shock. Therefore, the term CER may be inappropriate, and Puckett *et al.* (1995) named this wave pattern ARE, as illustrated in figure 1(*g*). From figures 1(*f*) and 1(*g*), one can conclude that the wave patterns discovered by Grove & Menikoff (1990) and Puckett *et al.* (1995) should be the same type. The former discussed curved interfaces, while the latter focused on planar interfaces. Nourgaliev *et al.* (2005) studied the shock refraction at a 'fast–slow' interface, more clearly demonstrating the ARE pattern described by Grove & Menikoff (1990). However, Nourgaliev *et al.* (2005) failed to distinguish between ARE and CFR, and considered them as the same wave pattern. Actually, CFR involves the reflection of a weak shock behind the incident shock, while ARE involves the reflection of an expansion wave at the bottom of the incident shock, as indicated by figures 1(*e*) and 1(*g*). Through the analysis above, when a planar shock refracts at a sharp 'fast–slow' interface, the wave pattern will experience RRR → RRE → ARE transitions within the very weak incident shock group, and RRR → MRR → CFR transitions within the stronger incident shock group.

The discussion above focuses mainly on sharp interfaces, across which the material properties such as density or sound speed change abruptly. However, in real physical

https://doi.org/10.1017/jfm.2025.282 Published online by Cambridge University Press

situations, the incident shock may interact with contact surfaces, shear layers, diffusion layers or mixing layers. The physical quantities corresponding to these stratified fluids exhibit certain distributions (such as mass fraction or velocity). At the same time, the incident shock wave will also experience various reflections and refractions within the diffusion layer, leading to complex flow characteristics. Henderson (1967*b*) ignored the viscous mixing between flow streams, and assumed that the boundary layer was composed of thin parallel inviscid streams. He theoretically analysed the shock–boundary layer interactions, and found that the boundary layer belongs to the 'slow–fast' type. At the 'slow–fast' interface, the regular pattern that only reflects expansion waves was widely observed in experiments and numerical simulations (Babinsky & Harvey 2011; Matheis & Hickel 2015; Grossman & Bruce 2018; Xue *et al.* 2020). However, by using the shock polar method, Henderson (1967*b*) predicted two additional types of regular reflection patterns within the boundary layer, namely, one with reflected compression waves, and the other with both reflected compression and expansion waves. These two types of regular pattern, to the best of the authors' knowledge, have never been verified. In addition, the ignition problem in the interaction between a supersonic mixing layer and an oblique shock wave was investigated by Huete *et al.* (2015), who used shock dynamics methods (Whitham 1958; Buttsworth 1996) to solve the shape of the transmitted shock within the mixing layer. However, they focused on the behaviour of the transmitted shock within the mixing layer, without considering the behaviour of the reflected shock. Martínez-Ruiz *et al.* (2019) numerically investigated the interaction of an oblique shock wave with a shear layer, and found that the oblique shock fails to deflect both streams consistently and to provide balanced flow properties downstream under supercritical conditions. In this situation, the flow exhibits irregular configurations that display self-similar pseudo-steady behaviour in the absence of characteristic length scales. However, the shear layer was still regarded as an infinitely thin layer, and the effect of the shear layer thickness on the wave transitions was not discussed.

From previous works mentioned above, the refraction phenomena at a diffusive interface would be different from those at a sharp interface. However, studies on the shock refraction at the 'fast–slow' stratified interface, e.g. the interaction between shock wave and fuel interface, have been scarce until now. Whether the classical criteria can still describe the behaviour of shock refraction at the stratified interface needs exploration. In the present study, the refraction patterns at the air–SF_6 stratified interface are investigated numerically to explore the effects of the stratified interface on the shock structures. In the following, first the numerical methods are described. Then the shock refraction processes at sharp and diffusive interfaces are provided for comparison. Subsequently, the refraction process within the diffusion layer is described using the shock polar method. Finally, the conditions for the emergence of the new refraction pattern are derived theoretically and verified numerically.

2. Numerical method

2.1. *Governing equations and numerical schemes*

In the numerical simulations, the compressible multi-component Euler equations are solved. The effects of chemical reactions, gravity, viscosity and the surface tension of gases are all ignored. The equations can be written as

$$\frac{\partial \boldsymbol{U}}{\partial t}+\frac{\partial \boldsymbol{F}}{\partial x}+\frac{\partial \boldsymbol{G}}{\partial y}=0, \tag{2.1}$$

https://doi.org/10.1017/jfm.2025.282 Published online by Cambridge University Press

where $\boldsymbol{U}$, $\boldsymbol{F}$ and $\boldsymbol{G}$ represent the conserved vectors and the convective fluxes in the x- and y- directions, respectively:

$$\boldsymbol{U}=\begin{bmatrix}\rho Y_1\\ \vdots\\ \rho Y_{N_g}\\ \rho u\\ \rho v\\ \rho E\end{bmatrix},\quad \boldsymbol{F}=\begin{bmatrix}\rho u Y_1\\ \vdots\\ \rho u Y_{N_g}\\ \rho u^2+p\\ \rho uv\\ u(\rho E+p)\end{bmatrix},\quad \boldsymbol{G}=\begin{bmatrix}\rho v Y_1\\ \vdots\\ \rho v Y_{N_g}\\ \rho vu\\ \rho v^2+p\\ v(\rho E+p)\end{bmatrix}, \tag{2.2}$$

where ρ, E and p denote the density, total energy and pressure of the gas mixture, u and v are the velocity components in the x- and y-directions, and Y_i is the mass fraction of gas species $i=1,2,\ldots,N_g$, with N_g the total number of species. The ideal gas equation of state for the gas mixture is used to close the governing equations

$$p=\rho\overline{R}T, \tag{2.3}$$

where $\overline{R}$ is the specific gas constant of the mixture. The total energy is given by

$$E=\frac{p}{\rho(\gamma-1)}+\frac{1}{2}(u^2+v^2), \tag{2.4}$$

where γ is the specific heat ratio of the mixture.

The governing equations are solved using the upwind maximum-principle-satisfying space–time conservation element and solution element scheme (Shen *et al.* 2015, 2017; Shen & Wen 2016). The present upwind scheme inherits the advantages of the Courant number insensitive scheme, which helps to reduce numerical dissipation. A weighted biased averaging procedure limiter is used to suppress spurious oscillations in problems with very strong discontinuities. The OpenMP parallel computation technology is applied to enhance computational capacity. This method has been well validated in capturing shock waves and details of complex flow structures (Guan *et al.* 2018, 2022; Fan *et al.* 2019).

2.2. *Computational settings and method validation*

Figure 3(*a*) illustrates the computational domain used for simulations of quasi-steady refraction, where $H=30$ mm, $L_1=50$ mm and $L_2=40$ mm. The solid wall condition is applied to the lower boundary, while the open boundary conditions are applied to other boundaries. A planar incident shock travels from left to right, and interacts with an inclined flat air–SF_6 interface. The shock intensity, denoted by ξ_i, is given by the Rankine–Hugoniot conditions. The pressure ahead of the incident shock wave is uniformly set as $p_0=101\,325$ Pa. The densities of air and SF_6 are 1.17 kg m^{-3} and 5.89 kg m^{-3}, respectively. The specific heat ratios for air and SF_6 are 1.4 and 1.1, respectively.

The interface between the test and ambient gases is defined by an interface equation in terms of the mass fraction:

$$\begin{aligned} Y_{air}&=\frac{Y_{air,0}}{2}+\frac{Y_{air,0}}{2}\,\mathrm{erf}\left(\frac{1}{2C_i}\frac{f_I-\varphi_L-\varphi_R}{\sqrt{\mathrm{d}x\,\mathrm{d}y}}\right),\\ f_I&=-L_2+y_I\tan\omega_0,\\ \varphi_{L,R}&=x_I\mp\frac{\mathrm{d}x}{2}, \end{aligned} \tag{2.5}$$

where the variable C_i is used to depict the interface diffusion degree, $Y_{air,0}=1.0$ is the air mass fraction, f_I is the function of interface position, φ_L and φ_R are the left- and

https://doi.org/10.1017/jfm.2025.282 Published online by Cambridge University Press

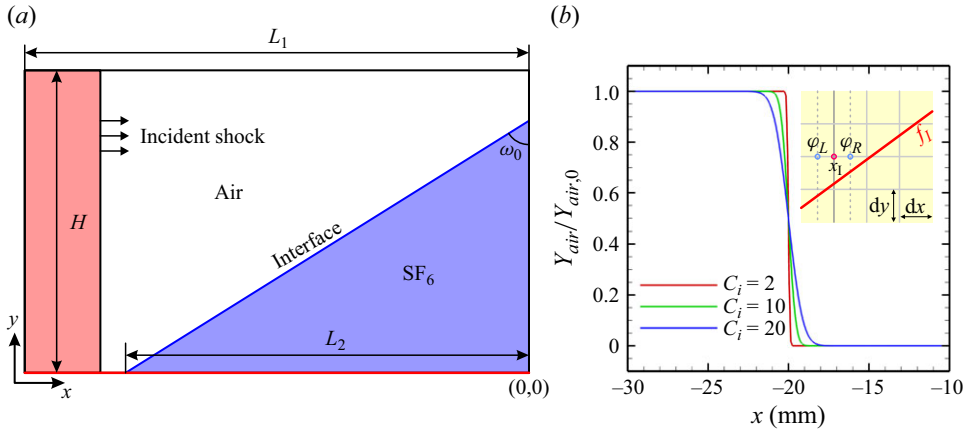


Figure 3. Schematic diagrams of (*a*) the computational domain and (*b*) the initial mass fraction distributions at $x = -20$ mm.

right-hand surfaces of the control volume, x_I and y_I are grid coordinates, and dx and dy represent the grid spacings in the x and y directions, respectively. In this work, the stratified interface results from diffusion caused by molecular thermal motion, without considering the specific distribution of physical quantities within the stratified interface. Three levels of diffusion, with the values of C_i being 2, 10 and 20, are considered. Their initial mass fraction distributions at $x = -20$ mm are shown in figure 3(*b*). The interface with $C_i = 2$ can be considered as a sharp one, while the interface with $C_i = 10$ or 20 is a diffusive one. Note that due to the inherent dissipation introduced by the discretisation of the governing equations in numerical computations, numerical schemes tend to smooth out sharp gradients. This means that even with $C_i = 2$ or smaller values, the interface cannot be guaranteed to be completely sharp, and will still spread to some extent. In addition, since the incident shock moves from left to right, the present set-up maintains a consistent degree of horizontal diffusion.

To clearly capture the shock structures and flow details, grid convergence validation is necessary. The interaction between a shock with $\xi_i = 0.25$ and an air–SF_6 interface is simulated numerically using four grid sizes: 0.2, 0.1, 0.05 and 0.025 mm. In these simulations, $\omega_0 = 30°$ and $C_i = 10$. Figure 4(*a*) provides the pressure contour of the numerical results, from which the shock structures and the interface become clearer with grid refinement. Figure 4(*b*) displays the density distribution along the line s_1s_2, which is convergent when the grid size is less than or equal to 0.05 mm. Considering both computational cost and the accuracy of the results, grid size 0.05 mm is adopted for subsequent calculations. In addition, to verify the reliability of the numerical program, the various shock angles when a shock refracts at a sharp interface ($C_i = 2$) between the present numerical results and the theoretical and experimental results from Abd-El-Fattah & Henderson (1978*a*) are compared in figure 5. Good agreement between them validates the reliability of the program in simulating the shock refraction process.

3. Shock refraction at the 'fast–slow' interface

3.1. *The sharp interface*

In this subsection, following the previous work of Abd-El-Fattah & Henderson (1978*a*), four different ξ_i, namely 0.909, 0.66, 0.25 and 0.143, corresponding to very weak, weak,

https://doi.org/10.1017/jfm.2025.282 Published online by Cambridge University Press

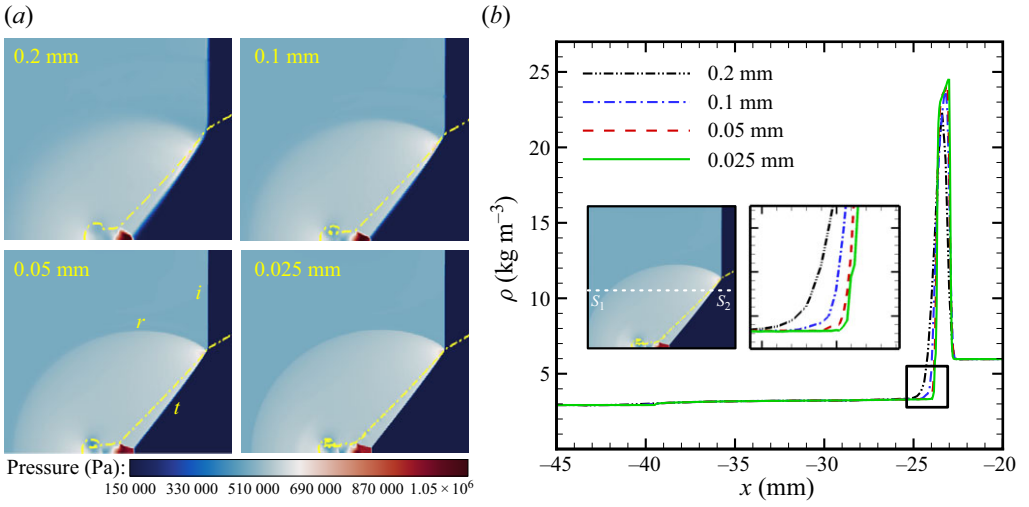


Figure 4. (*a*) Pressure contours of refraction patterns under different grid sizes, with $\xi_i = 0.25$, $\omega_0 = 30°$ and $C_i = 10$. (*b*) The density distributions along the line s_1s_2 under different grid sizes.

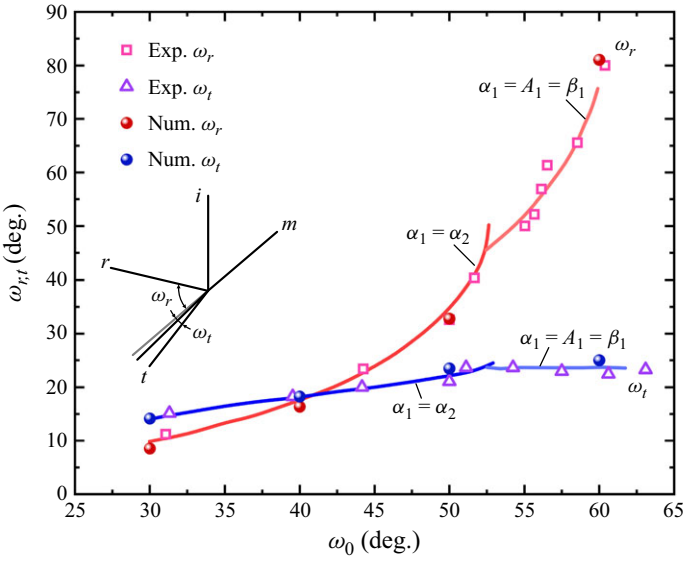


Figure 5. Comparison of the shock angles between the present numerical results (circular symbols) and the theoretical (lines) and experimental (triangular symbols) results of Abd-El-Fattah & Henderson (1978*a*) when a planar shock with $\xi_i = 0.25$ refracts at the air–SF_6 interface. Here, ω_r (ω_t) is the angle between the reflected shock (transmitted shock) and the initial interface. The squares and triangles represent the experimental results, while the circular symbols represent the present numerical results.

strong and stronger incident shocks, respectively, are adopted. For each ξ_i, four specific incident angles $\omega_0 = 50$ °, 60°, 70° and 80° are selected for simulations.

Figure 6 illustrates the shock refraction patterns at the sharp air–SF_6 interface depicted by the pressure contour. The case $\xi_i = 0.909$ is discussed first. When $\omega_0 = 50°$, the reflection wave is a shock wave, and the incident, reflected and transmitted shocks intersect at the same point on the interface, creating a typical RRR structure. As ω_0 gradually

https://doi.org/10.1017/jfm.2025.282 Published online by Cambridge University Press

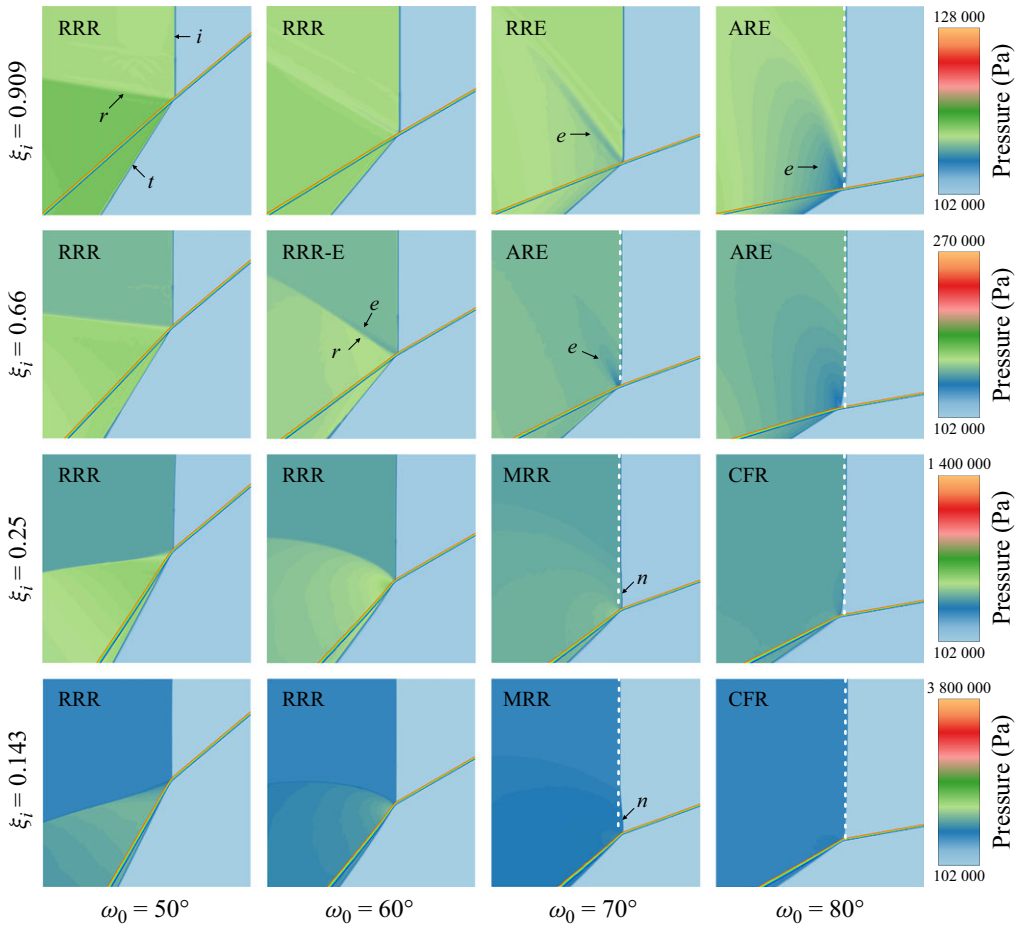


Figure 6. Pressure contours of the shock refracting at the air–SF_6 interface with $C_i = 2$.

increases, the reflected shock is weakened, eventually degenerating into a Mach line. When ω_0 increases to 70°, the reflected wave becomes an expansion wave, and the refraction pattern is RRE. As $\omega_0 = 80°$, the refraction pattern transitions to ARE. The bottom of the incident shock in ARE has not undergone significant bending, and a central expansion wave region is present behind the incident shock. Within the very weak shock group, there are no new refraction phenomena at these four isolated moments, and the refraction patterns at the sharp interface in the present work are consistent with those described in the classical refraction process.

When $\xi_i = 0.66$ and $\omega_0 = 50°$, the refraction pattern at the interface is RRR. However, when ω_0 becomes 60°, a new refraction phenomenon occurs at the interface, with an additional wave appearing ahead of the reflected shock. The pressure contour lines at this moment are provided in figure 7(*a*), and the dimensionless pressure extracted along the line x_1x_2 across the reflected wave is plotted in figure 7(*b*). From x_1 to x_2, the dimensionless pressure first decreases, influenced by the additional wave, and then increases, caused by the reflected shock. Therefore, this additional wave appearing ahead of the reflected shock is an expansion wave. If the criterion $Y_{air} = 0.99$ is considered as the interface position, then the incident shock and the reflected shock no longer meet at the same point on the interface due to the spacing of the expansion wave. Based on this special phenomenon,

https://doi.org/10.1017/jfm.2025.282 Published online by Cambridge University Press

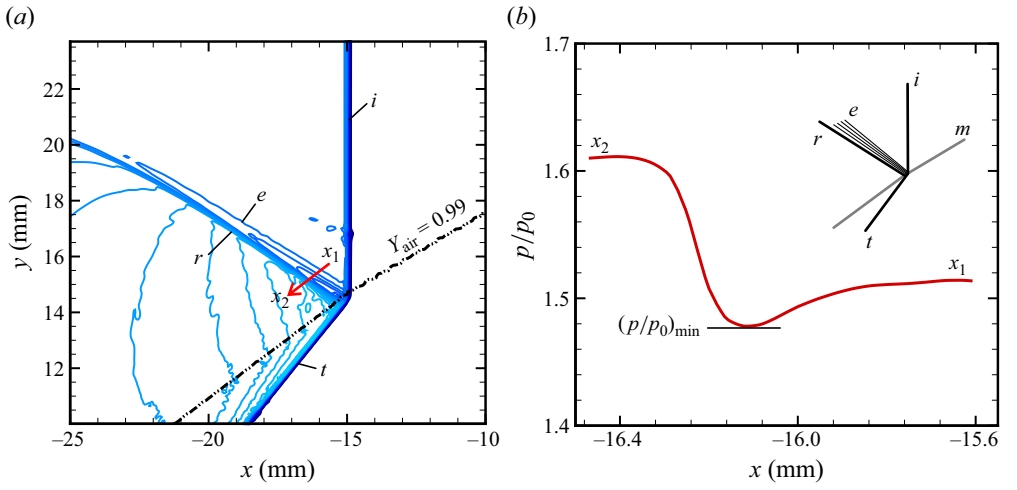


Figure 7. (*a*) The pressure contour lines of the RRR-E structure at $\xi_i = 0.25$ and $\omega_0 = 60°$. (*b*) The dimensionless pressure distribution along the line x_1x_2.

it is named RRR-E in the present work, referring to the regular refraction where a low-pressure expansion wave region exists between the incident shock and the reflected shock. The reason for the occurrence of RRR-E will be discussed in the next section. When ω_0 reaches 70°, the reflected wave completely turns into an expansion wave. The head of the central expansion wave gradually detaches and propagates along the incident shock, forming a non-central expansion wave band. The refraction pattern at the moment was referred to as ARE (Grove & Menikoff 1990; Puckett *et al.* 1995). At $\omega_0 = 80°$, the bottom of the incident shock wave has been affected by the expansion wave. As a result, within the weak incident shock group, the refraction patterns in the present work evolve from RRR to RRR-E and then to ARE as ω_0 increases. However, in the previous studies, it was commonly accepted that the refraction patterns at the interface would experience the RRR $\rightarrow$ MRR $\rightarrow$ CFR transitions as ω_0 increases within the weak incident shock group.

When the incident shock intensity is within the strong and stronger groups, the refraction pattern becomes MRR at $\omega_0 = 70°$. The Mach stem n is not distinct, and it protrudes slightly forwards. At $\omega_0 = 80°$, the wave system becomes CFR, where the reflected wave has degenerated, and the part of the incident shock wave near the interface curves away from the wave, which is consistent with the results of Nourgaliev *et al.* (2005).

3.2. *The diffusive interface*

Figures 8 and 9 display the numerical results of a planar shock refraction at air–SF_6 interfaces with different degrees of diffusion. Under the conditions $\xi_i = 0.909$ and $\omega_0 = 50°$, RRR-E is produced at the two diffusive interfaces, while RRR is generated at the sharp interface, as shown in figure 6. As a result, the diffusion at the interface increases the likelihood of the appearance of RRR-E. The pressure contour lines of RRR and RRR-E at $\xi_i = 0.909$ and $\omega_0 = 50°$ conditions are compared in figure 10. One can observe that for the sharp interface, the reflected wave is strictly a shock. For the diffusion interface with $C_i = 10$, however, the reflected shock wave in the vicinity of the interface has degenerated into a series of compression waves under the influence of a reflected expansion wave, although the reflected wave away from the interface is still a shock. As ω_0 continues to increase, the refraction patterns at the diffusive interface are the same as those at the sharp interface.

https://doi.org/10.1017/jfm.2025.282 Published online by Cambridge University Press

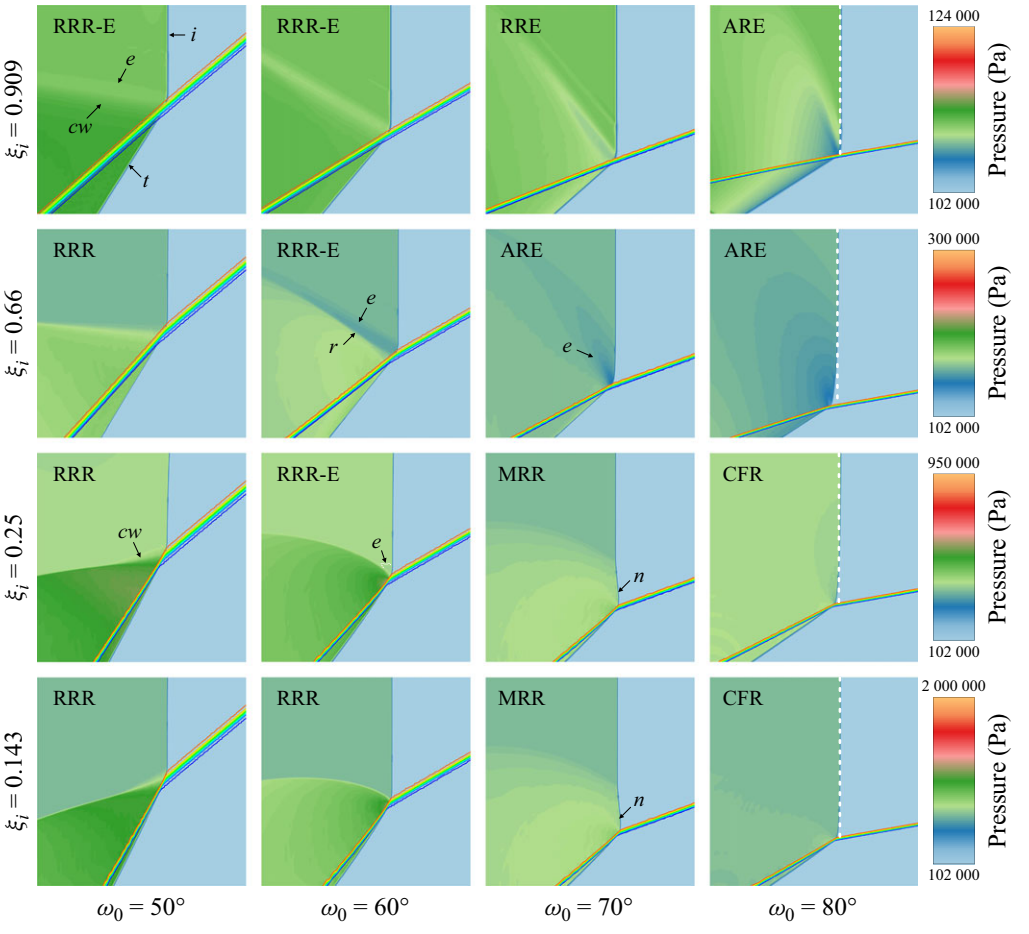


Figure 8. Pressure contours of the shock refracting at the diffusion air–SF_6 interface with $C_i = 10$. Here, cw indicates compressible wave.

When $\xi_i = 0.25$ and $\omega_0 = 50°$, due to the interface diffusion, the compression waves are reflected from different positions, and the wavefronts of the compression waves eventually merge into a shock. When ω_0 increases to 60°, an expansion wave e exists between the incident and reflected shocks, which may be considered as the moment of the RRR $\rightarrow$ RRR-E transition. As ω_0 increases further, the expansion wave disappears, and the RRR-E $\rightarrow$ MRR transition occurs. Subsequently, the refraction processes at the diffusive interface are the same as those at the sharp interface.

To sum up, the diffusion of the interface leads to the emergence of RRR-E in the refraction process. This is manifested by the fact that there is an expansion wave between the incident shock and the reflected shock. As the degree of the interface diffusion increases, RRR-E will appear in a broader parameter space. Note that Henderson (1967*b*) theoretically predicted that both reflected expansion and compression waves may occur when a shock wave collides with a 'slow–fast' boundary layer, but there has been no experimental or numerical evidence until now. The present work verifies numerically that both reflected compression and expansion waves can be generated simultaneously when a shock refracts at a 'fast-slow' interface under certain conditions (figure 10*b*), which provides indirect evidence to the theory of Henderson (1967*b*). Moreover, the present work

https://doi.org/10.1017/jfm.2025.282 Published online by Cambridge University Press

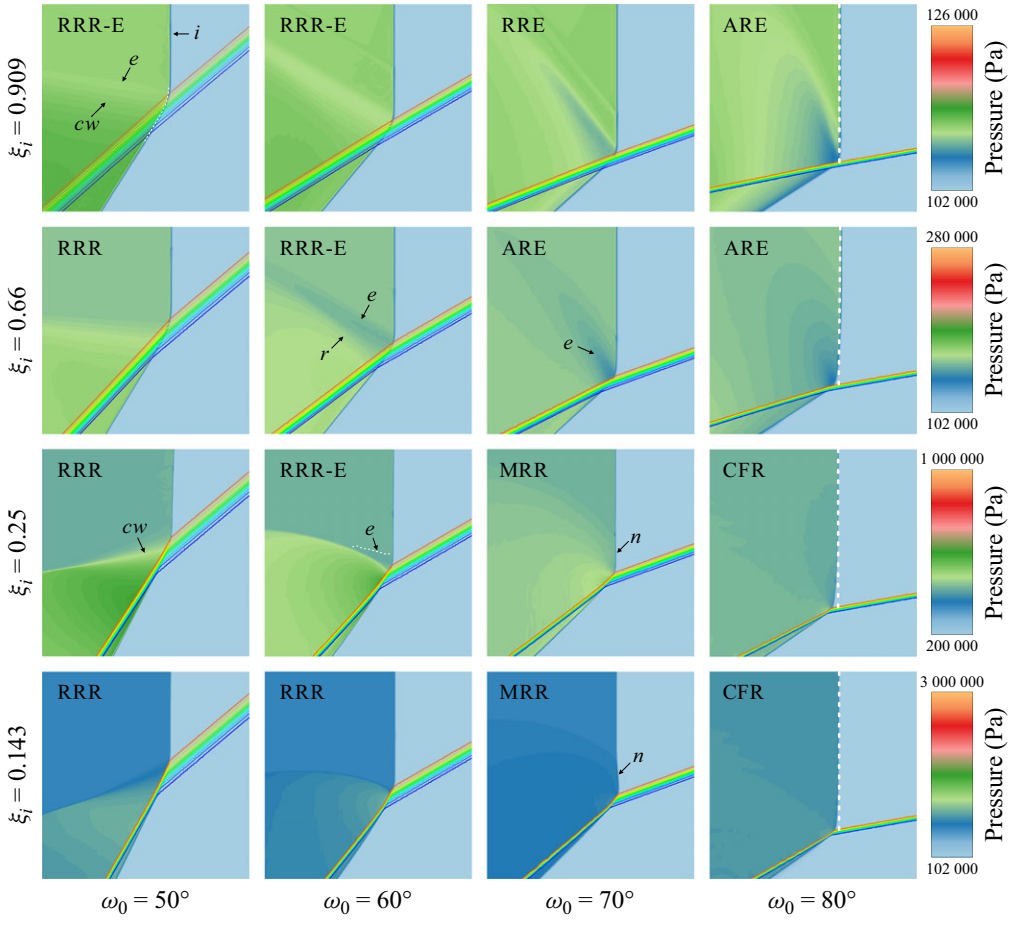


Figure 9. Pressure contours of the shock refracting at the diffusion air–SF_6 interface with $C_i = 20$.

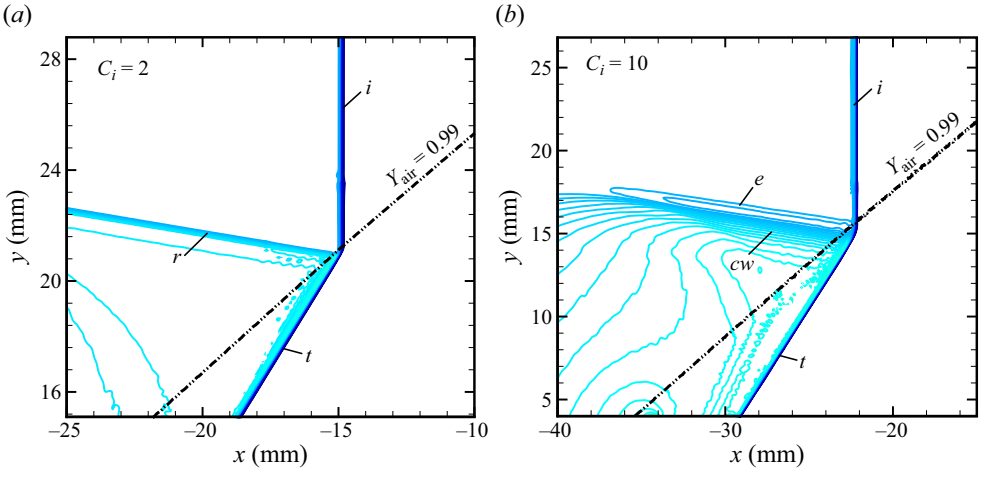


Figure 10. The pressure contour lines of (*a*) RRR and (*b*) RRR-E structures at $\xi_i = 0.909$ and $\omega_0 = 50°$.

https://doi.org/10.1017/jfm.2025.282 Published online by Cambridge University Press

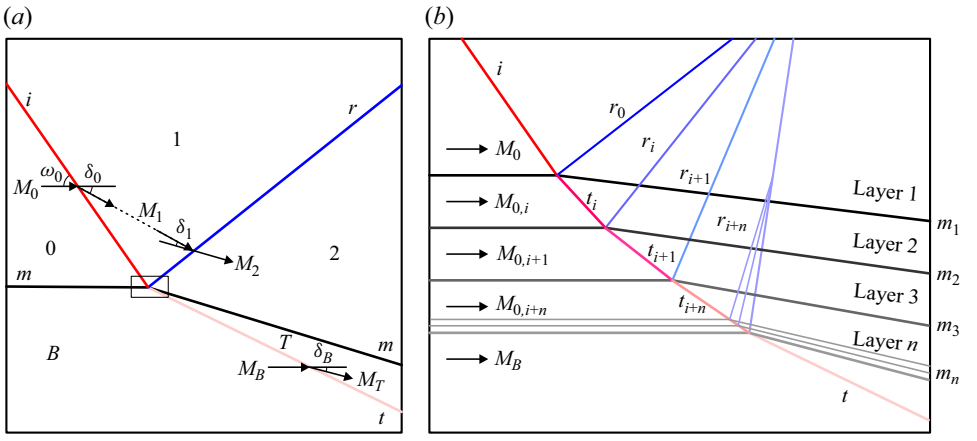


Figure 11. Schematic diagrams of (*a*) the classical shock refraction process and (*b*) the shock refraction process in the local diffusion layer.

finds that the reflected compression waves will then merge into a shock wave, forming RRR-E.

In the extreme case where the interface is perfectly sharp, RRR-E should be absent, but it is observed at the interface with $C_i = 2$. This is because the interface width in the computations is discretised by a finite number of grid cells, and the numerical schemes tend to dissipate sharp interfaces. This results in a certain distribution of the physical properties across a finite number of grids. As a result, the interface in the computations is not strictly sharp, resulting in RRR-E formation.

4. Analysis of shock refraction in the diffusion layer

4.1. *Shock polar method*

In the classic shock refraction problem, as shown in figure 11(*a*), the interface is typically considered as an infinitely thin plane membrane with negligible mass, separating two gases that are generally of different compositions. Meanwhile, these gases initially share the same temperature and pressure, and each gas is assumed to fill half of an infinite space. It is also assumed that the entire motion is steady and two-dimensional. If the reflected wave is a shock, then the following equations can be derived from ordinary one-dimensional gas dynamics:

$$\tan\delta_{0,1,B} = \frac{(p_{1,2,T}/p_{0,1,B}) - 1}{1 + \gamma_{0,1,B} M_{0,1,B}^2 - (p_{1,2,T}/p_{0,1,B})} \times \left(\frac{\dfrac{2\gamma_{0,1,B}}{\gamma_{0,1,B}+1} M_{0,1,B}^2 - \dfrac{\gamma_{0,1,B}-1}{\gamma_{0,1,B}+1} - (p_{1,2,T}/p_{0,1,B})}{\dfrac{\gamma_{0,1,B}-1}{\gamma_{0,1,B}+1} + (p_{1,2,T}/p_{0,1,B})} \right)^{1/2}, \tag{4.1}$$

$$\frac{1 + \frac{1}{2}(\gamma_0 - 1) M_0^2}{1 + \frac{1}{2}(\gamma_0 - 1) M_1^2} = \frac{\dfrac{\gamma_0 - 1}{\gamma_0 + 1} + (p_1/p_0)}{\dfrac{\gamma_0 - 1}{\gamma_0 + 1} + (p_0/p_1)}, \tag{4.2}$$

https://doi.org/10.1017/jfm.2025.282 Published online by Cambridge University Press

where γ and M represent the specific heat ratio and the flow Mach number, respectively. The subscripts 0, 1 and 2 represent the gas states ahead of the incident shock, behind the incident shock, and behind the reflected shock, respectively. The subscripts B and T represent the gas states ahead of and behind the transmitted shock.

Under equilibrium conditions, the velocities of the incident and transmitted shocks will be equal along the interface, therefore $v_0 = v_B$. The speed of sound is given by $a_{0,\mathrm{B}} = [\gamma_{0,\mathrm{B}}\, RT_{0,\mathrm{B}}/\mathcal{M}_{0,\mathrm{B}}]^{1/2}$, where R is the universal gas constant, and $\mathcal{M}$ is the molecular weight. Since the temperature is $T_0 = T_B$, the relation between the flow Mach numbers upstream of the incident and transmitted shocks can be obtained as

$$M_B = M_0 \left[\frac{\gamma_0 \mathcal{M}_B}{\gamma_B \mathcal{M}_0}\right]^{1/2}. \tag{4.3}$$

In addition, the following continuity conditions need to be satisfied at the interface:

$$\delta_B = \delta_0 + \delta_1, \tag{4.4}$$

$$p_T/p_B = (p_1/p_0)(p_2/p_1). \tag{4.5}$$

If the reflected wave is an expansion wave, then the Prandtl–Meyer relations will be adopted as follows:

$$\begin{aligned}\theta_1 = {} & \sqrt{\frac{\gamma_0+1}{\gamma_0-1}}\arctan\sqrt{\frac{\gamma_0-1}{\gamma_0+1}\left(M_2^2-1\right)} - \arctan\sqrt{M_2^2-1} \\ & - \sqrt{\frac{\gamma_0+1}{\gamma_0-1}}\arctan\sqrt{\frac{\gamma_0-1}{\gamma_0+1}\left(M_1^2-1\right)} + \arctan\sqrt{M_1^2-1}.\end{aligned} \tag{4.6}$$

Accordingly, (4.4) is modified as follows:

$$\delta_B = \delta_0 + \theta_1. \tag{4.7}$$

Equations (4.1)–(4.5) can be transformed into a single polynomial equation of degree 12 with p_T/p_B as the variable. Through the discussion on the real roots of the equation, a complete description of the refraction wave system can be obtained. However, if the reflected wave is an expansion wave, then it is difficult to simplify (4.6) into an algebraic equation due to its transcendental nature. Nevertheless, the shock polar method can be used to find the desired solution. As shown in figure 12(*a*), when $\xi_i = 0.909$ and $\omega_0 = 68°$, the polar envelope of the transmitted shock is outside the polar envelope of the incident shock. To satisfy the pressure equilibrium behind the reflection wave and the transmitted shock, a reflected expansion wave is needed. The expansion wave polar originates from point E_1 on the incident shock polar, which represents the state behind the incident shock, and intersects with the transmitted shock polar at point C. From equations, one can calculate $\delta_0 = 1.38°$ and $\delta_B = 1.49°$. When $\xi_i = 0.25$ and $\omega_0 = 50°$, as shown in figure 12(*b*), the reflected shock polar extends from point D_2 on the incident shock polar and intersects with the transmitted shock polar at points α_1 and α_2 to match the pressure relationship. Generally, the weaker solution α_1 occurs, and correspondingly, $\delta_0 = 24.54°$ and $\delta_B = 17.20°$.

However, if the interface has a diffusion layer, then the physical properties of the gas within the layer exhibit a certain distribution. When an incident shock impinges such a diffusion layer, to satisfy the conditions required by (4.3), the velocities within the diffusion layer should also exhibit a certain velocity distribution to match the velocities v_0 and v_B outside the diffusion layer, as shown in figure 11(*b*). Thus it can be assumed that the flow Mach number varies continuously and monotonically from M_0 to M_B.

https://doi.org/10.1017/jfm.2025.282 Published online by Cambridge University Press

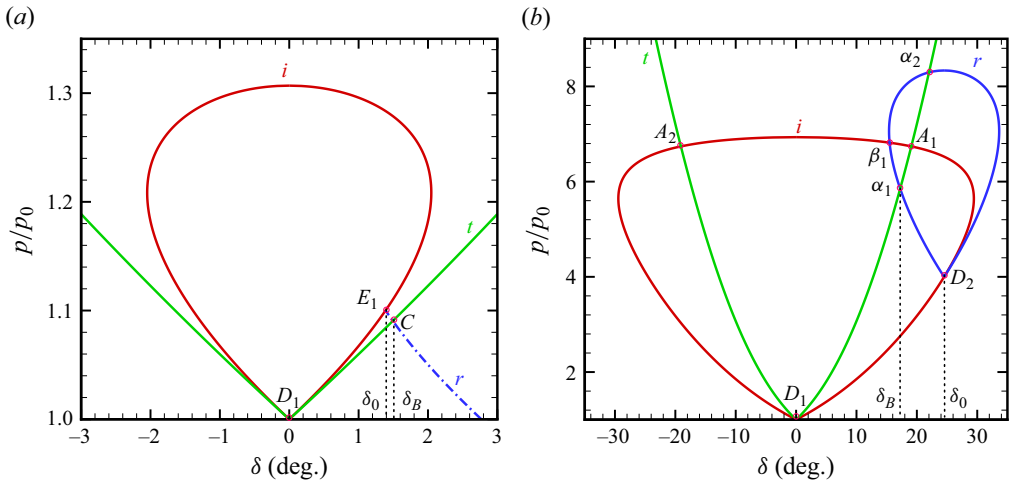


Figure 12. Polar diagrams showing the shock refraction at the air–SF_6 interface (*a*) in the very weak incident shock group with $\xi_i = 0.909$ and $\omega_0 = 68°$, and (*b*) in the strong incident shock group with $\xi_i = 0.25$ and $\omega_0 = 50°$. Here, D_1 and D_2 are double solution points; A_1 and A_2 are intersection points of the incident shock and the transmitted shock polars; α_1 and α_2 are intersection points of the reflected shock and the transmitted shock polars; C is the intersection point of the reflected expansion and the transmitted shock polars; E_1 is the intersection point of the reflected expansion and the incident shock polars; and β_1 is the intersection point of the reflected shock and the incident shock polars.

Since the acoustic impedance of SF_6 is greater than that of air, it follows that $M_{0,i} < M_{0,i+1} < M_{0,i+n}$. For analytical convenience, the continuous distribution of flow Mach number is approximated by an incremental profile, assuming that the diffusion layer consists of thin parallel streams of inviscid gas with minimal changes in flow Mach number between the streams. This assumption neglects the effect of viscous mixing between the streams. If the incident shock wave (i) strikes the edge of this diffusion layer, as shown in figure 11(*b*), then it will be refracted by the increment change of the flow Mach number. Consequently, a transmitted shock wave t_i will emerge, along with a reflected shock or expansion wave r_0. At the next Mach number increment, the transmitted wave t_i itself will be refracted, leading to the emergence of a transmitted shock t_{i+1}, accompanied by a reflected wave r_i. Subsequently, t_{i+1} will continue to produce t_{i+2}, t_{i+3}, t_{i+n} in the new gas layers. Throughout the refraction process, a series of reflected waves r_i, r_{i+1}, r_{i+n} will be emitted within the diffusion layer, and the nature of these reflected waves needs to be determined based on the properties of the local gas. From (4.3), what actually affects the increment of the flow Mach number is the ratio of specific heat γ and the molecular weight $\mathcal{M}$. To intuitively explore the effect of the diffusion layer on the refraction process, it is assumed that there are four gas interfaces (m_1, m_2, m_3, m_4) within the diffusion layer, as shown in figure 11(*b*). These four interfaces represent a gradual transition of physical properties from one gas to another, and can effectively demonstrate the possibilities of wave formation within the diffusion layer. This assumption is made to simplify the problem and to allow for a step-by-step analysis of the refraction process within the diffusion layer. In fact, at least two gas interfaces are required, and more gas interfaces could more accurately reflect the physical state of the waves (such as pressure and flow deflection angles) in the diffusion layer. Although this assumption is not fully rigorous, it is a common approach in numerical and theoretical studies to discretise continuous regions into manageable elements for analysis. On both sides of each interface, there are uniform gas layers with specific heat ratios and molecular weight ratios as listed in table 1. In the

https://doi.org/10.1017/jfm.2025.282 Published online by Cambridge University Press

	γ	$\mathcal{M}$
Layer 1	1.40	28.97
Layer 2	1.33	58.23
Layer 3	1.25	87.49
Layer 4	1.18	116.74
Layer 5	1.10	146.00

Table 1. Parameters of specific heat ratio γ and molecular weight $\mathcal{M}$ for different diffusion layers.

following, the interactions between an incident shock with $\xi_i = 0.66$ and four interfaces with ω_0 of 60° and 30°, respectively, will be discussed, and the formation mechanism of RRR-E will be explored.

Figures 13(*a*) and 13(*b*) illustrate the refraction of the incident shock within the diffusion layer under the conditions $\xi_i = 0.66$ and $\omega_0 = 60°$. When the incident shock interacts with the interface m_1, the flow deflection angle behind the incident shock δ_{00} can be determined. However, at this deflection angle, the polar envelope of the transmitted shock is outside the polar envelope of the incident shock, indicating that the pressure behind the incident shock is higher than that behind the transmitted shock. Therefore, a reflected expansion wave is required to match the pressure relationship. The expansion wave polar r_1 is originated from a point on the incident shock polar, intersecting with the transmitted shock polar at the point RE_1. When the transmitted shock t_1 generated from the interface m_1 becomes the incident shock and impinges the interface m_2, the flow deflection angle δ_{01} can be determined. At this point, the polar envelope of the transmitted shock t_2 is inside the polar envelope of t_1, indicating that the pressure behind the incident shock (t_1) is less than that behind the transmitted shock (t_2). Therefore, a reflected shock is needed to match the pressure relationship. The reflected shock polar r_2 is produced from point RE_1 on the polar t_1, intersecting with the polar t_2 at point RS_2. The interactions between the transmitted shock and subsequent interfaces only produce shocks, which gradually superimpose to form a stronger shock. The appearance of the expansion wave polar r_1 creates an interesting structure where the reflected waves include both an expansion wave and a shock. As a result, the present work theoretically verifies that both expansion wave and shock wave can be generated simultaneously when a shock refracts at a 'fast–slow' interface.

However, if ω_0 changes to 30°, as shown in figures 13(*c*) and 13(*d*), then when the incident shock interacts with the interface m_1, the transmitted shock polar intersects with the reflected shock polar at point RS_1. From this point on, all interactions between the transmitted shock and the interfaces will reflect shocks. These shocks gradually superimpose to form a stronger reflected shock. There is no expansion wave between the incident and reflected shocks.

4.2. *Theoretical analysis of refraction modes in the diffusion layer*

From the analysis in § 4.1, it can be concluded that the generation of an expansion wave is represented in the shock polar diagram as the intersection of the transmitted shock polar and the reflected expansion wave polar. However, it is not rigorous to assume the diffusion layer as a finite number of thin parallel inviscid gas layers, as it is difficult to accurately find the conditions that exactly produce an expansion wave. To predict the conditions of RRR-E formation, it is necessary to seek answers on the shock polar diagrams. As shown in figure 12(*a*), there is a double solution D_1 between the transmitted shock polar and the incident shock polar, and there will also be two single solutions A_1 and A_2 under certain

https://doi.org/10.1017/jfm.2025.282 Published online by Cambridge University Press

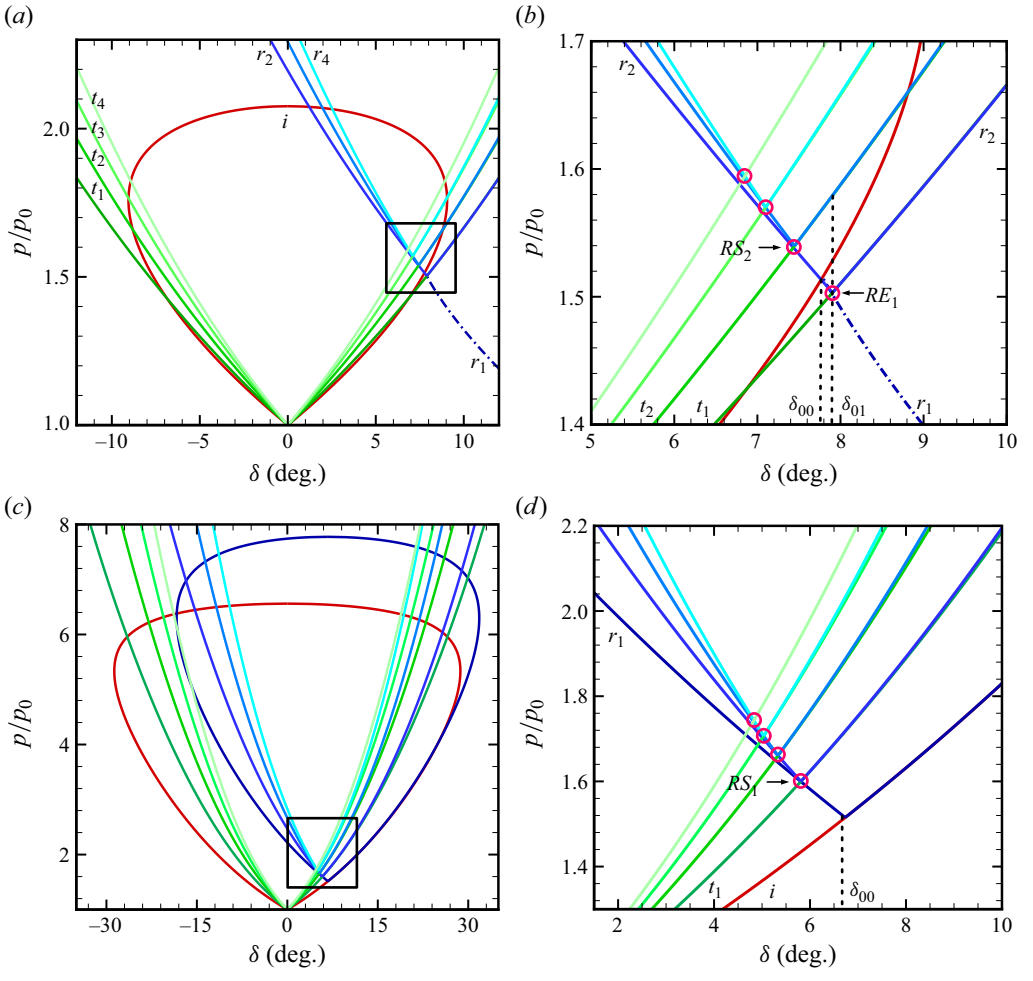


Figure 13. Polar diagrams showing the refraction of a planar shock with $\xi_i = 0.66$ at the diffusive air-SF_6 layer, for (a,b) $\omega_0 = 60°$ and (c,d) $\omega_0 = 30°$. Here, RE (RS) is the intersection of the reflected expansion wave polar (reflected shock polar) with the transmitted shock polar; and δ_{00} and δ_{01} are the flow deflection angles caused by the incident shock and the expansion wave, respectively.

conditions, as shown in figure 12(*b*). The reflected shock or expansion wave polar has a double solution D_2 with the incident shock polar. An expansion wave can be generated only when A_1 and A_2 have no solutions, as shown in figure 12(*a*), or the ordinate values of A_1 and A_2 are less than that of D_2, as shown in figure 13(*b*). In fact, the case of A_1 and A_2 having no solutions is actually a special case where the ordinate values of A_1 and A_2 approach that of D_1 infinitely. It is more general to analyse the case where the ordinate values of A_1 and A_2 are less than that of D_2. Since the ordinate values of A_1 and A_2 are the same, and only A_1 has physical significance in the present analysis, A_2 will not be discussed in subsequent analyses.

The ordinate value of A_1 ($\epsilon = p_{1,T_i}/p_{0,B_i}$) can be obtained by solving (4.1):

$$\tan\delta_{0,B_i} = \frac{\epsilon - 1}{1 + \gamma_{0,B_i} M_{0,B_i}^2 - \epsilon} \times \left(\frac{\dfrac{2\gamma_{0,B_i}}{\gamma_{0,B_i}+1} M_{0,B_i}^2 - \dfrac{\gamma_{0,B_i}-1}{\gamma_{0,B_i}+1} - \epsilon}{\dfrac{\gamma_{0,B_i}-1}{\gamma_{0,B_i}+1} + \epsilon} \right)^{1/2}. \tag{4.8}$$

https://doi.org/10.1017/jfm.2025.282 Published online by Cambridge University Press

It is worth noting that when the incident shock interacts with the diffusion interface, the physical properties of the gas within the diffusion layer must be distributed in some manner, which inevitably affects the propagation of the shock. However, in the present analysis, it is simply assumed that the velocity within the layer varies monotonically, without specifying a particular distribution form (such as Gaussian or exponential). Therefore, it is impossible to accurately determine the variation of the pressure ratio within the diffusion layer. Actually, the pressure ratio ϵ in (4.8) only corresponds to the conditions required for the formation of the RRR-E pattern near the air side (ambient gas). As a result, the pressure ratio in the diffusion layer may only affect the transmitted shock behaviour, but does not affect the formation conditions of the RRR-E pattern. For the convenience of mathematical operations, the relevant variables in the above equation are substituted:

$$\begin{aligned}
&\delta_0 = \delta_{B_i}, \quad p_1/p_0 = p_{T_i}/p_{B_i}, \\
&a_1 = 1 + \gamma_0 M_0^2, \quad a_2 = 1 + \mu\gamma_0 M_0^2, \\
&b_1 = \frac{2\gamma_0 M_0^2}{\gamma_0 + 1} - \frac{\gamma_0 - 1}{\gamma_0 + 1}, \quad b_2 = \frac{2\mu\gamma_0 M_0^2}{\gamma_{B_i} + 1} - \frac{\gamma_{B_i} - 1}{\gamma_{B_i} + 1}, \\
&c_1 = \frac{\gamma_0 - 1}{\gamma_0 + 1}, \quad c_2 = \frac{\gamma_{B_i} - 1}{\gamma_{B_i} + 1},
\end{aligned} \tag{4.9}$$

where $\mu = \mathcal{M}_{B_i}/\mathcal{M}_0$. Then from (4.8) and (4.9), it can be derived that

$$\frac{(a_2 - \epsilon)^2}{(a_1 - \epsilon)^2} = \frac{(b_2 - \epsilon)}{(c_2 + \epsilon)} \frac{(b_1 - \epsilon)}{(c_1 + \epsilon)}. \tag{4.10}$$

In previous work (Henderson 1967*b*), only the variation in flow Mach number was involved, but the effect of the specific heat ratio was ignored, resulting in a single algebraic equation of degree 2. However, in the present discussion, the effects of both the specific heat ratio and the molecular weight ratio of the gases are considered simultaneously, hence resulting in a single polynomial equation of degree 3 with $\epsilon = p_{T_i}/p_{B_i}$ as the variable:

$$\chi_1 \epsilon^3 + \chi_2 \epsilon^2 + \chi_3 \epsilon + \chi_4 = 0, \tag{4.11}$$

where χ_1, χ_2, χ_3 and χ_4 are the coefficients, which can be expressed as

$$\begin{aligned}
\chi_1 &= -2a_1 + 2a_2 + b_1 - b_2 + c_1 - c_2, \\
\chi_2 &= a_1^2 - a_2^2 - 2a_2 b_1 + 2a_1 b_2 - 2a_1 c_1 - b_2 c_1 + 2a_2 c_2 + b_1 c_2, \\
\chi_3 &= a_2^2 b_1 - a_1^2 b_2 + a_1^2 c_1 - a_2^2 c_2 + 2a_1 b_2 c_1 - 2a_2 b_1 c_2, \\
\chi_4 &= -a_1^2 b_2 c_1 + a_2^2 b_1 c_2.
\end{aligned} \tag{4.12}$$

Although there is a general solution for the polynomial equation of degree 3, its expression is too complex, and a computer program is utilised to solve (4.11). From the expressions of (4.12), the variation of ϵ is controlled by the ratio of specific heats γ_{B_i} and the molecular weight ratio μ of the gas layers. Therefore, solutions are sought in the parameter space where the specific heat ratio γ_{B_i} ranges from 1.1 to 1.9, and the molecular weight ratio μ varies between 1.05 and 3 (the solutions will diverge when μ is too small). The computational results are provided in figure 14. Note that during the calculation, when the imaginary part of the solution is less than 1×10^{-5}, it is considered as 0, thus the solution is regarded as a real root. In addition, the results shown in figure 14 are from one of the solutions to (4.12), while the other two solutions are discarded because they involve imaginary roots.

https://doi.org/10.1017/jfm.2025.282 Published online by Cambridge University Press

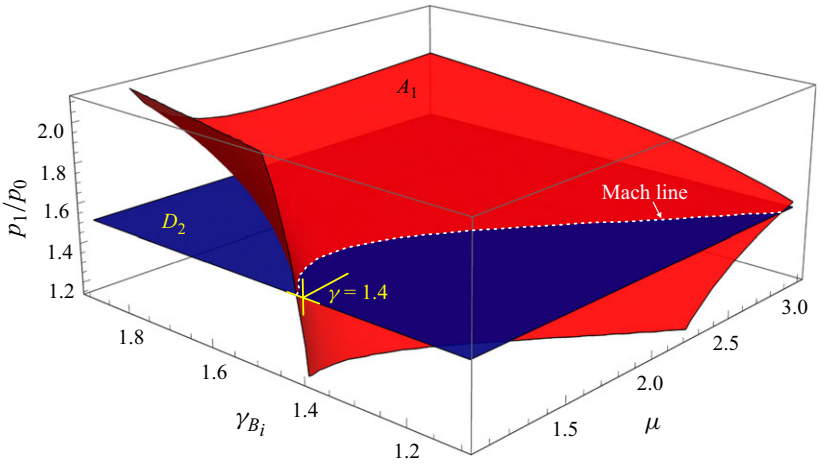


Figure 14. The distribution of parameter space for single solution A_1 and double solution D_2 at $\xi_i = 0.66$ and $\omega_0 = 60°$. The blue surface represents the distribution of the double solution D_2, and the red surface represents the distribution of the single solution A_1. The white dashed line represents the distribution of Mach lines.

In figure 14, the red surface represents the parameter space in which the incident and transmitted shock polars in the diffusion layer intersect at the single solution point A_1. The blue surface represents the intersection point D_2 of the incident shock polar with the reflected wave polar within the diffusion layer. The white dashed line indicates the limit situation where the reflected shock degenerates into a Mach line. It can be observed that on one side of the Mach line, the value of A_1 is greater than that of D_2, and the pressure behind the incident shock is less than that behind the transmitted shock. To match the pressure difference, a reflected shock wave is generated from the interface. On the other side, the value of A_1 is less than that of D_2, and therefore an expansion wave is reflected, forming RRR-E. Moreover, the physical properties in the diffusion layer should transition continuously from air to SF_6. On the side close to air, the acoustic impedance of the gas in the diffusion layer is similar to air, making it possible for an expansion wave to form at the interface, as shown in figure 13. As one moves closer to SF_6 within the diffusion layer, the properties of the gas become more like those of SF_6, making it easier to produce a shock wave at the interface. Therefore, RRR-E can form only when the specific heat ratio γ is close to 1.4, and the value of A_1 is less than that of D_2. Here, we should emphasise that the RRR-E pattern in the present work forms only when the specific heat ratio γ is close to 1.4, because the ambient gas is air with specific heat ratio 1.4. If the ambient gas is helium with specific heat ratio 1.66, then the RRR-E pattern would form when γ is close to 1.66. As a result, the RRR-E pattern is not a fairly rare phenomenon. Due to the divergence of solutions at $\mu = 1$ and $\gamma = 1.4$, the numerical magnitudes of A_1 and D_2 are assessed at $\mu = 1.02$ and $\gamma = 1.4$ to determine whether RRR-E will form or not.

To verify the accuracy of the aforementioned model, the phase diagram showing the refraction patterns at an air–SF_6 interface is plotted in figure 15. The red triangles calculated by (4.11) represent the critical solutions of the RRR $\rightarrow$ RRR-E transition. Because the method through figure 14 requires us to judge whether there is a possibility of generating RRR-E or not under certain initial conditions, the red triangles in figure 15 are all discrete points. In order to compare with the phase diagram of the sharp interface, the discrete computational results are fitted to obtain the equation

$$\xi_i = 1.72 \times 10^{-3}\omega_0^2 - 0.24\omega_0 + 8.13. \tag{4.13}$$

https://doi.org/10.1017/jfm.2025.282 Published online by Cambridge University Press

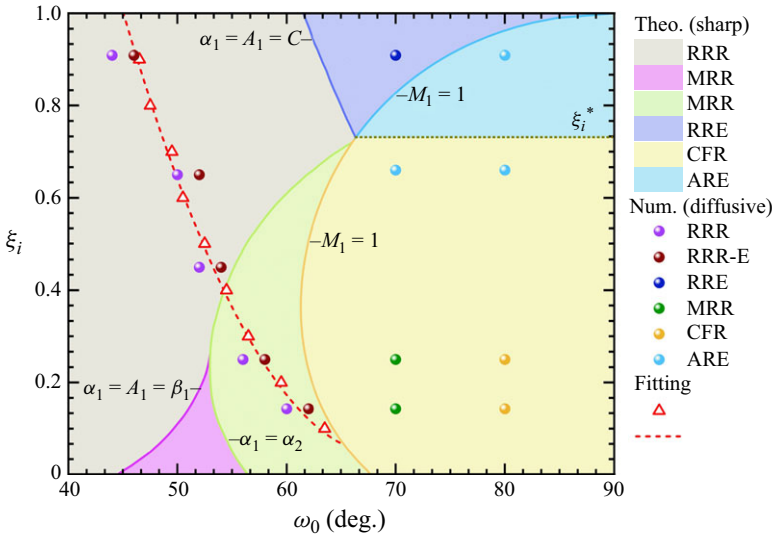


Figure 15. The phase diagram showing the refraction patterns. All the solid lines are derived from Abd-El-Fattah & Henderson (1978*a*), representing the boundaries between refraction patterns at a sharp interface. The different regions enclosed by these solid lines are indicated by different colours, representing the various refraction patterns at the sharp interface obtained theoretically. All the circular symbols come from the present numerical results. The triangles represent the results calculated using (4.11). The red dashed line is the fitted boundary between RRR and RRR-E calculated by (4.13).

All circular symbols in figure 15 represent the numerical results at $C_i = 10$. The purple and brown circular symbols represent RRR and RRR-E, respectively. Both these symbols are well distributed on either side of the transition line described by (4.13), which demonstrates that the present model can reasonably predict the conditions for the emergence of RRR-E. All the solid lines are derived from Abd-El-Fattah & Henderson (1978*a*), representing the boundaries between refraction patterns at a sharp interface. The different regions enclosed by these solid lines are indicated by different colour blocks, representing the various refraction patterns at the sharp interface obtained theoretically. The orange and blue solid lines are obtained based on the condition $M_1 = 1$. In the previous work (Abd-El-Fattah & Henderson 1978*a*), the authors considered all refraction patterns to the right of $M_1 = 1$ as CFR. In fact, a distinction should be made at one ξ_i^*, as shown in figure 15, where for $\xi_i > \xi_i^*$, the refraction pattern to the right of $M_1 = 1$ should be ARE, and when $\xi_i < \xi_i^*$, it should be CFR. For the air–SF_6 interface, the value of ξ_i^* is approximately 0.73.

At a sharp interface, it is commonly accepted that MRR will occur in the region between $\alpha_1 = A_1 = \beta_1$ and $\alpha_1 = \alpha_2$, and the region between $\alpha_1 = \alpha_2$ and $M_1 = 1$. However, at the diffusion interface, the transition line described by (4.13) crosses through the later region, and MRR even occurs in the region to the right of $M_1 = 1$. This indicates that the appearance of MRR is delayed due to the emergence of RRR-E. This is of significant value for the structural design of the combustion chamber in scramjet engines. When considering the interaction between shock waves and fuel, the fuel interface cannot be simply regarded as an infinitely thin layer, and the diffusion effect should be considered. Overall, the shock refraction at the diffusive interface is accompanied by the emergence of new phenomena, and the existing transition laws for sharp interfaces are no longer accurate.

https://doi.org/10.1017/jfm.2025.282 Published online by Cambridge University Press

5. Conclusions

The quasi-steady shock refraction at a diffusive air–SF_6 interface is investigated in the present work. The effects of shock intensity, incident angle and diffusion thickness on the refraction patterns are highlighted. A new refraction pattern, named RRR-E, where both shock and expansion waves are present simultaneously in the reflected waves, is first observed at the diffusive interface in the numerical simulations, but it is not expected to occur in shock refraction at a sharp interface. The RRR-E pattern is characterised by the presence of an expansion wave between the incident and reflected shocks, with the initiation points of the incident and reflected shock waves not being at the same position. Due to the presence of RRR-E, the transition processes of different refraction patterns at the diffusive 'fast–slow' interface are different from those at the sharp interface.

The mechanism of RRR-E formation is analysed qualitatively using the shock polar method. The results show that because the physical properties of gases in the diffusion layer present a certain distribution, continuous refraction processes occur within the diffusion layer to satisfy the kinematic relationship between the reflected wave and the transmitted shock. This results in the formation of RRR-E at the diffusive interface if the initial conditions are appropriate. Subsequently, the conditions for the occurrence of RRR-E are obtained theoretically and verified by numerical results. In the phase diagram of the refraction patterns, the presence of RRR-E results in the transition boundaries of different refraction patterns at the sharp interface being no longer valid. Specifically, the emergence of RRR-E delays the Mach refraction (MRR) process, which is of great significance for the design of scramjet engines.

However, the present work only provides the conditions for the formation of RRR-E, i.e. the transition boundary from the regular refraction with a reflected shock to RRR-E. The transition boundaries from RRR-E to the regular refraction with a reflected expansion wave or to MRR are still unclear, which need further investigation. In addition, the diffusive layer in the present numerical simulations is established based on different physical properties; the effects of other quantities, such as the velocity distribution within the stratified fluids, on the refraction process still require clarification.

Funding. This work was supported by the National Natural Science Foundation of China (nos 12388101 and 12372281), the Strategic Priority Research Program of Chinese Academy of Sciences (no. XDB0620201) and Youth Innovation Promotion Association CAS.

Declaration of interests. The authors report no conflict of interest.

References

ABD-EL-FATTAH, A.M. & HENDERSON, L.F. 1978*a* Shock waves at a fast–slow gas interface. *J. Fluid. Mech.* **86** (1), 15–32.

ABD-EL-FATTAH, A.M. & HENDERSON, L.F. 1978*b* Shock waves at a slow–fast gas interface. *J. Fluid. Mech.* **89** (1), 79–95.

ARUN KUMAR, R., RAJESH, G. & JAGADEESH, G. 2022 The reflection and refraction of a curved shock front sliding over an air–water interface. *Shock Waves* **32** (6), 497–515.

BABINSKY, H. & HARVEY, J.K. 2011 *Shock Wave–Boundary-Layer Interactions*. Cambridge University Press.

BEN-DOR, G., IGRA, O. & ELPERIN, T. 2000 *Handbook of Shock Waves*. Elsevier.

BUTTSWORTH, D.R. 1996 Interaction of oblique shock waves and planar mixing regions. *J. Fluid. Mech.* **306**, 43–57.

DELMONT, P., KEPPENS, R. & VAN DER HOLST, B. 2009 An exact Riemann-solver-based solution for regular shock refraction. *J. Fluid. Mech.* **627**, 33–53.

ELIAS, P.Q. *et al.* 2018 Improving supersonic flights with femtosecond laser filamentation. *Sci. Adv.* **4** (11), eaau5239.

https://doi.org/10.1017/jfm.2025.282 Published online by Cambridge University Press

FAN, E., GUAN, B., WEN, C. & SHEN, H. 2019 Numerical study on the jet formation of simple-geometry heavy gas inhomogeneities. *Phys. Fluids* **31** (2), 026103.
GICHON, Y., JOSE, J.T., CHANDRAVAMSI, H., EVRON, Y. & RAM, O. 2024 The dynamics of shock wave propagation far downstream of an abrupt area expansion. *J. Fluid. Mech.* **997**, A30.
GROSSMAN, I.J. & BRUCE, P.J. 2018 Confinement effects on regular–irregular transition in shock-wave–boundary-layer interactions. *J. Fluid. Mech.* **853**, 171–204.
GROVE, J.W. & MENIKOFF, R. 1990 Anomalous reflection of a shock wave at a fluid interface. *J. Fluid. Mech.* **219**, 313–336.
GUAN, B., LIU, Y., WEN, C. & SHEN, H. 2018 Numerical study on liquid droplet internal flow under shock impact. *AIAA J.* **56** (9), 3382–3387.
GUAN, B., YANG, H., YANG, H. & WANG, G. 2022 On the irregular jet formation of shock-accelerated spherical heavy gas bubbles. *Phys. Fluids* **34** (12), 126111.
HAN, Z. & YIN, X. 1993 *Shock Dynamics*. Kluwer Academic Publishers and Science Press.
HENDERSON, L.F. 1966 The refraction of a plane shock wave at a gas interface. *J. Fluid Mech.* **26** (3), 607–637.
HENDERSON, L.F. 1967*a* On expansion waves generated by the refraction of a plane shock at a gas interface. *J. Fluid Mech.* **30** (2), 385–402.
HENDERSON, L.F. 1967*b* The reflexion of a shock wave at a rigid wall in the presence of a boundary layer. *J. Fluid Mech.* **30** (4), 699–722.
HUETE, C., SÁNCHEZ, A.L., WILLIAMS, F.A. & URZAY, J. 2015 Diffusion-flame ignition by shock-wave impingement on a supersonic mixing layer. *J. Fluid Mech.* **784**, 74–108.
LUO, X., WANG, M., SI, T. & ZHAI, Z. 2015 On the interaction of a planar shock with an SF_6 polygon. *J. Fluid Mech.* **773**, 366–394.
MARKHOTOK, A. & POPOVIC, S. 2010 Refractive phenomena in the shock wave dispersion with variable gradients. *J. Appl. Phys.* **107** (12), 123302.
MARKHOTOK, A., POPOVIC, S. & VUSKOVIC, L. 2008 The boundary effects of the shock wave dispersion in discharges. *Phys. Plasmas* **15** (3), 032103.
MARTÍNEZ-RUIZ, D., HUETE, C., MARTÍNEZ-FERRER, P.J. & MIRA, D. 2019 Irregular self-similar configurations of shock-wave impingement on shear layers. *J. Fluid Mech.* **872**, 889–927.
MATHEIS, J. & HICKEL, S. 2015 On the transition between regular and irregular shock patterns of shock-wave/boundary-layer interactions. *J. Fluid Mech.* **776**, 200–234.
NOURGALIEV, R.R., SUSHCHIKH, S.Y., DINH, T. & THEOFANOUS, T.G. 2005 Shock wave refraction patterns at interfaces. *Intl J. Multiphase Flow* **31** (9), 969–995.
POLACHEK, H. & SEEGER, R.J. 1951 On shock-wave phenomena; refraction of shock waves at a gaseous interface. *Phys. Rev.* **84** (5), 922–929.
PUCKETT, E.G., HENDERSON, L.F. & COLELLA, P. 1995 A general theory of anomalous shock refraction. In *Shock Waves@ Marseille IV: Shock Structure and Kinematics, Blast Waves and Detonations*, pp. 139–144. Springer.
RAJ, C.A.S., PRASAD, S.V., RAJESH, G. & SAMEEN, A. 2024 Pseudosteady shock refractions over an air–water interface. *J. Fluid Mech.* **998**, A49.
SABNIS, K. & BABINSKY, H. 2023 A review of three-dimensional shock wave–boundary-layer interactions. *Prog. Aerosp. Sci.* **143**, 100953.
SHEN, H. & WEN, C. 2016 A characteristic space–time conservation element and solution element method for conservation laws II. Multidimensional extension. *J. Comput. Phys.* **305**, 775–792.
SHEN, H., WEN, C., PARSANI, M. & SHU, C. 2017 Maximum-principle-satisfying space–time conservation element and solution element scheme applied to compressible multifluids. *J. Comput. Phys.* **330**, 668–692.
SHEN, H., WEN, C. & ZHANG, D. 2015 A characteristic space–time conservation element and solution element method for conservation laws. *J. Comput. Phys.* **288**, 101–118.
SZUBERT, D., GROSSI, F., GARCIA, A.J., HOARAU, Y., HUNT, J.C. & BRAZA, M. 2015 Shock-vortex shear-layer interaction in the transonic flow around a supercritical airfoil at high Reynolds number in buffet conditions. *J. Fluids Struct.* **55**, 276–302.
TAKAYAMA, K. & BEN-DOR, G. 1989 Pseudo-steady oblique shock wave reflections over water wedges. *Exp. Fluids* **8** (3–4), 129–136.
TAUB, A.H. 1947 Refraction of plane shock waves. *Phys. Rev.* **72** (1), 51–60.
URZAY, J. 2018 Supersonic combustion in air-breathing propulsion systems for hypersonic flight. *Annu. Rev. Fluid Mech.* **50** (1), 593–627.
VON NEUMANN, J. 1963 *Oblique Reflection of Shock Waves; Collecttion Works*, vol. 6, pp. 238–299. Pergamon Press.

https://doi.org/10.1017/jfm.2025.282 Published online by Cambridge University Press

WHEATLEY, V., PULLIN, D. & SAMTANEY, R. 2005 Regular shock refraction at an oblique planar density interface in magnetohydrodynamics. *J. Fluid Mech.* **522**, 179–214.

WHITHAM, G.B. 1958 On the propagation of shock waves through regions of non-uniform area or flow. *J. Fluid Mech.* **4** (4), 337–360.

XUE, L., SCHRIJER, F.F., VAN OUDHEUSDEN, B., WANG, C., SHI, Z. & CHENG, K. 2020 Theoretical study on regular reflection of shock wave–boundary layer interactions. *J. Fluid Mech.* **899**, A30.

YANG, H. & RADULESCU, M.I. 2021 Dynamics of cellular flame deformation after a head-on interaction with a shock wave: reactive Richtmyer–Meshkov instability. *J. Fluid Mech.* **923**, A36.

ZHAI, Z., LI, W., SI, T., LUO, X., YANG, J. & LU, X. 2017 Refraction of cylindrical converging shock wave at an air/helium gaseous interface. *Phys. Fluids* **29** (1), 016102.

ZHAI, Z., WANG, M., SI, T. & LUO, X. 2014 On the interaction of a planar shock with a light polygonal interface. *J. Fluid Mech.* **757**, 800–816.

ZHANG, E., LIAO, S., ZOU, L., ZHAI, Z., LIU, J. & LI, X. 2024 Refraction of a triple-shock configuration at planar fast–slow gas interfaces. *J. Fluid Mech.* **984**, A49.

https://doi.org/10.1017/jfm.2025.282 Published online by Cambridge University Press